Performance Improvement of Proton Exchange Membrane Fuel Cells Through Numerical Investigation of a Tapered Flow Field Configuration

Binyamin[1,2] and Ocktaeck Lim[3(✉)]

[1] Graduate School of Mechanical Engineering, University of Ulsan, Ulsan 44610, Republic of Korea
bin279@umkt.ac.id
[2] Department of Mechanical Engineering, Universitas Muhammadiyah Kalimantan Timur, Samarinda, Indonesia
[3] Department of Mechanical Engineering, University of Ulsan, Ulsan 44610, Republic of Korea
otlim@ulsan.ac.kr

Abstract. Tapered flow field configurations (FFCs) improve oxygen transport, water removal, and proton exchange membrane fuel cell performance. A three-dimensional multi-phase fuel cell model is used to quantify how the tapered FFC affects the internal physicochemical process and cell performance. The tapered FFC is compared without and with PMT and TCR. The tapered FFC with PMT and TCR increases oxygen delivery, water removal, and cell performance. In tapered FFCs with PMT and TCR, a more excellent $L_{I/O}$ ratio initially enhances but later worsens oxygen transport, water removal, and cell efficiency. Low $L_{I/O}$ ratios reduce cell performance regardless of FFC taper. The best tapered FFC design with a $L_{I/O}$ of 1.2 has more homogeneous reactant and current density profiles than other tapered FFC designs, decreasing the current density and oxygen mass fraction variation coefficient and improving cell performance.

Keywords: PEM fuel cell · tapered FFC · Thermal contact resistance · fuel cell performance

1 Introduction

Due to energy shortages and fossil fuel pollution, alternative energy sources are essential. Due to its high power density and minimal emissions, the proton exchange membrane fuel cell (PEMFC) has recently garnered international attention. PEMFC quickly converts fuel chemical energy into electricity, unlike heat engines. Without the Carnot cycle, it can generate power at 40–60% efficiency. PEMFC produces solely water and heat, making it environmentally friendly. PEMFC is a leading choice for distributed power production, portable power sources, and hybrid vehicles due to its benefits [1–3]. PEMFC commercialization requires a model to estimate total performance. Designers

T. P. Syawitri et al. (Eds.): MEST 2022, AER 222, pp. 220–240, 2023.
https://doi.org/10.2991/978-94-6463-134-0_21

can optimize operational settings after assessing PEMFC performance. Fuel cells include multiple physicochemical processes, which complicates standard modeling. Analytical and mechanical fuel cell models require knowledge of process parameters and physical phenomena [4].

The PEM fuel cell's cathode flow field architecture (FFC) allows for effective mass transport and water removal, uniform dispersion of internal physical quantities, reduced pressure drop, high production yields, and a cheap cost [5–7]. PEM fuel cell FFCs are parallel, serpentine, or engaged. Reactants migrate from gas diffusion layers (GDLs) into the catalyst layer (CL) in the parallel FFC, mostly due to concentration differences [6]. Nonetheless, this type of FFC creates an inadequate supply of reactant and low water removal at high current densities, resulting in reactant starvation in the reaction site and reactant maldistribution inside fuel cells, lowering cell efficiency [5]. In serpentine and interdigitated FFC porous electrodes, concentration diffusion and forced convention affect reactant transport. Thus, they enable effective water removal and generally homogeneous reactant distributions [5, 8]. These FFCs have substantial pressure drops, which reduce pumping loss and energy efficiency [8]. Finally, in PEM fuel cells, serpentine, parallel, and engaged FFCs have pros and cons.

To solve the concerns mentioned, substantial research has been done on the change of standard FFCs with different cross-section forms [9, 10], lengths and channel aspect ratios [11, 12], baffle conditions [13, 14], and convergent [15], wave-like [16, 17], tapered [18–21], and sub-channel [18]. Kuma et al. [9] reported that hemispherical and triangular cross-sections improved fuel cell performance. Cooper et al. [12] tested the channel length-to-width ratio of a fuel cell with an engaged flow field. The high aspect ratio flow field accumulated more water. Guo et al. [22], Wang et al. [13], and Yin et al. [14] investigated parallel FFC fuel cell baffles. Baffles enhanced reactant distribution uniformity, eliminated extra liquid water with a smaller voltage drop, and increased optimum net power density over the standard FFC. Chen et al. [16]created a fuel cell 3D wave flow channel. According to simulations, the optimal design improved cell performance by enhancing liquid water removal and reactant gas flow inside electrodes. Xu et al. [18] studied the tapered FFC. Aspect ratio and sidewall angle substantially affected channel flow dispersion. Parallel cathode flow routes now have sub-inlets. With low channel pressure, a proper sub-inlet position and a fair volume of dry air may boost water removal and cell performance [23]. An array of laser holes was bored into the cathode flow field cathode by Whiteley et al. [24] to create a "Through Planar Array" (TPA) FFC. This novel FFC improved cell performance by increasing mass diffusion and water removal at greater current densities with lower back pressure.

In addition, the number of studies on creating new FFCs continues to rise. His FFC designs for honeycomb [25], spiral [26], concentric spiral [27], cylindrical [28] and conical tube [29]. Atyabi and Afshari [25] created a honeycomb-shaped FFC for PEM fuel cells. According to numerical calculations, his FFC with honeycomb geometry provides a homogeneous distribution of variables comparable to multi-channel meandering flow fields and a minimal pressure drop comparable to straight parallel flow fields. Jang et al. [26] computed their PEM fuel cell numerically with spiral channels. Secondary vortices were discovered to be produced using a spiral channel layout. That enhances heat and mass transmission in curved channels, enhancing cell performance. Meanwhile, G. Cai

et al. [30] presented a design influenced by natural waves for the flow field of PEM fuel cells. They found that the current density could be increased in specific flow fields while the pressure loss was much reduced. A unique honeycomb-like flow channel design was presented by Zhang et al. [31]. The honeycomb-like flow channel was superior to more traditional methods in performance and oxygen non-uniformity. The other study suggested a literature assessment of natural-structure-based flow fields by Iranzo et al. [32]. Several variations of serpentine flow channels were proposed by Zhang et al. [31]. Researchers discovered that cells with more uniform current densities performed better when their bends did not intersect. To quantitatively analyze the effect of different blockage cross-section types on mass transfer processes and cell performance, Y. Cai et al. [33] developed a PEMFC model with a straight channel. The data suggested that using a trapezoidal cross-section model improved cell performance.

In this study's research, a tapered parallel FFC was designed for fuel cells at both the anode and cathode BPs to improve mass transfer, water removal, and overall cell efficiency. The PMT and TCR application in the innovative FFC is investigated using a three-dimensional multi-phase PEM fuel cell model. The model focuses on the relationship between the BPs and GDLs. The influence of the intake side length ratio to that of the outlet ($L_{I/O}$) in the new FFC is examined by examining the dispersion of internal physical quantities inside the porous electrodes of fuel cells. That allows for a better understanding of the relationship between the two. The coefficients of variables such as the liquid water saturation, oxygen mass fraction, current density, and dissolved water content characterize these quantities. This study aims to determine the uniform distributions of the internal physical characteristics of fuel cells, which will improve their overall efficiency.

2 Development of Fuel Cell Model

Illustrative of a PEM fuel cell with standard parallel FFCs and tapered parallel FFCs are shown in Fig. 1 (a) and 1 (b). The components of a PEM fuel cell in a conventional parallel FFC, the ribs and channels' height, width, and length are 2, 2, and 40 mm, respectively. Table 1 shows what the PEM fuel cell looks like in terms of its shape. In tapered parallel FFCs, the tapered form changes both the cathode and anode BPs. In this work, seven different types of tapered FFCs are made, each with a different ratio ($L_{I/O}$) of the length of the intake side to the length of the outlet side. In this computer-based study, $L_{I/O}$ 0.2, $L_{I/O}$ 0.4, $L_{I/O}$ 0.6, $L_{I/O}$ 0.8, $L_{I/O}$ 1.0, and $L_{I/O}$ 1.2 tapered parallel FFCs will be looked at computationally. Different tapered parallel FFCs will, of course, have very other contact surfaces between BPs and GDLs.

Numerous studies [39, 40] demonstrate that TCR is directly proportional to contact area. Consequently, the PMT and the TCR variation must be considered for different tapered parallel FFCs. In general, the ECR between BPs and GDLs can be determined using [36]:

$$R_C = \frac{1}{\sum_{i=1}^{n} \frac{1}{R_i}} + \frac{1}{\sum_{i=1}^{n} \frac{S_i}{A\left(B/p_n^i\right)^C}} \tag{1}$$

Table 1. Conventional PEMFC geometric parameters.

No.	Parameters	Value	Unit
1	Channel length	40.0	mm
2	Channel height	1.0	mm
3	Channel width	1.0	mm
4	Rib width	1.0	mm
5	Cell width	2.0	mm
6	GDL thickness	0.3	mm
7	CL thickness	0.014	mm
8	Membrane thickness	0.12	mm

Table 2. For ordinary parallel and other tapered parallel FFCs, TCR dan PMT between BPs and GDLs.

Case No.	Description	PMT (m)	TCR (W/m^2K)
1	$L_{I/O}$ 0.2	0.0	0.0
2	$L_{I/O}$ 0.4	0.000015	0.0001
3	$L_{I/O}$ 0.6	0.00002	0.0025
4	$L_{I/O}$ 0.8	0.000025	0.005
5	$L_{I/O}$ 1.0	0.00003	0.075
6	$L_{I/O}$ 1.2	0.000035	0.1

where Rc is the interfacial TCR total and represents the amount of contact areas, Ri and Si are the ith contact element's interfacial TCR and boundary area, respectively; pi n is the normal contact stress component, and Constant coefficients A, B, and C According to Wang, et al. [21] study PEMFC with tapered FCs used some parameters such, A = 81.4 m cm2, B = 2.52 MPa, C = 1.07, and pi n = 1.52 MPa [37] in this simulation. The computed PMT and TCR between GDLs and BPs for various traditional and tapered parallel FFCs are shown in Table 2.

2.1 Computational Domain and Assumption

Figure 1 (a–c) depicts Mesh and domain for computations using the tapered parallel fuel cell. Since the tapered parallel FFC fuel cell is symmetrical, this simulation's mathematical model consists of a single channel and rib. A multi-zone technique divides the computational region using a hexahedral mesh, having 544,000 mesh components. The fuel cell model in this study was created using the two-fluid approach under the following assumptions:

1. It is assumed that the mixing gas is ideal and that the flow through the channel is continuous, incompressible, and laminar.
2. It is anticipated that the channel will have a homogeneous mist flow, so the liquid velocity within the flow channels is about equivalent to the gas velocity.
3. Considered homogenous and isotropic are the porous electrodes and polymer membrane.
4. The water in the polymer membrane is in the dissolving phase.
5. The conditions of a fuel cell remain constant regardless of gravity.
6. Gas diffusion and liquid water transport inside porous electrodes are described by Fick's law, the Leverett J-function, and the Wyllie model.
7. The electrochemical reactions within CLs are described using the Bulter-Volmer equation.

2.2 Conservation Equations

There are eight conservation equations in the exhaustive description of the fuel cell's heat, mass, and charge transport properties. For energy, mass, momentum, species, transport of liquid and dissolved water, and transport of protons and electrons, the following conservation equations are supplied. In each zone of a PME fuel cell, the conservation of energy equation is solved:

$$\nabla \bullet \left(\varepsilon s \rho_1 C_{\mathrm{p,l}} u_l T + \varepsilon(1-s)\rho_g C_{p,\mathrm{g}} u_g T\right) = \nabla \bullet \left(\mathrm{k}^{eff}\, \nabla \mathrm{T}\right) + S_T \tag{2}$$

CHs, GDLs, and CLs all deal with mass and momentum conservation equations:

$$\nabla \bullet \left(\frac{1}{\varepsilon(1-s)} \rho_g \overrightarrow{u_g}\right) = S_m \tag{3}$$

$$\nabla \bullet \left(\frac{1}{\varepsilon^2(1-s)^2} \rho_g \overrightarrow{u_g}\,\overrightarrow{u_g}\right) = -\nabla p_g + \nabla \bullet \left(\frac{1}{\varepsilon(1-s)} \mu_g \nabla \overrightarrow{u_g}\right) + S_u \tag{4}$$

In CHs, GDLs, and CLs, the conservation equations for species diffusion are solved:

$$\nabla \bullet \left(\frac{1}{\varepsilon(1-s)} \rho_g \overrightarrow{u_g} X_k\right) = \nabla \bullet \left(\rho_g D_k^{eff} \nabla X_k\right) + S_k \tag{5}$$

where k represents oxygen, hydrogen, nitrogen, and water vapor, the problem of transfer of liquid water is resolved using CHs, GDLs, and CLs:

$$\nabla \bullet \left[\frac{\rho_l k_{kl} K}{\mu_g} \frac{\partial \rho_c}{\partial \mathrm{s}} \nabla \mathrm{s}\right] = S_l + \nabla \bullet \left[\frac{\rho_l k_{kl} K}{\mu_l} \nabla p_g\right] \tag{6}$$

CLs and MEM address the dissolved water conservation equation:

$$\frac{\rho_{\mathrm{mem}}}{EW} \nabla \bullet (\mathrm{D}_\lambda \nabla_\lambda) - \nabla \bullet \left(\frac{n_{\mathrm{d}}\, \overrightarrow{i}_{\mathrm{mem}}}{F}\right) = S_d \tag{7}$$

In CLs and the MEM, the conservation of proton transport is resolved:

$$\nabla \bullet \left(K_{mem}^{eff} \nabla \phi_{\text{mem}} \right) + \text{S}_{\text{mem}} = 0 \tag{8}$$

In CLs and the MEM, the conservation of proton transport is determined:

$$\nabla \bullet \left(K_{e}^{eff} \nabla \phi_{\text{e}} \right) + \text{S}_{\text{e}} = 0 \tag{9}$$

2.3 Physical Transport Correlation, Source Terms, and Essential Conservation Equation Factors

For example, the Bruggeman correlation [38] can be used to determine the gas effective diffusion coefficient; the model of Leverett J-function and Wyllie's [39] can be used to determine the diffusivity of liquid water transport; Motupally et al. [40] can determine the diffusivity of dissolved water transport; the Butler-Volmer equation [41] can be used to determine the rate of an electrochemical reaction; and the conductivity of protons reported by Springer et al. [42]. The model's conservation equations for the various forms of physicochemical transport are tabulated in Table 3. Tables 4 and 5 show the current PEM fuel cell model's design, transport, and operational parameters and the source terms for the conservation above equations.

2.4 Boundary Condition

Several needed boundary conditions are established to solve the created PEM fuel cell's partial differential equations. Anode and cathode CH inlet borders, for instance, are defined by the mass flow rate, which can be calculated as follow:

$$m_a = \frac{\rho_a \xi_a i_{ref} A_r}{2F} \frac{RT}{p_a - RH_a p^{sat}} \tag{10}$$

$$m_c = \frac{\rho_c \xi_c i_{ref} A_r}{4F} \frac{RT}{0.21(p_c - RH_c p^{sat})} \tag{11}$$

The molar concentration of gas species can be determined by controlling for humidity, operating pressure, and temperature. Exterior walls, as well as anode and cathode inlets, were maintained at a steady 343.15 K. The pressure outlet boundaries with no molar concentrations of species were chosen as the limits of the anode and cathode CHs. All momentum, mass, species, and liquid water flows were stopped at the GDL/BP and MEM/CL interfaces. Nonetheless, at the MEM/CL interface, charge, heat, and dissolved water were transported using coupled boundary conditions. In contrast, at the GDL/BP interface, the electronic phase and heat were transported using coupled boundary conditions. Zero voltage and the working potential were applied to the anode and cathode current collectors, respectively.

2.5 Numerical Methodology

In the computational fluid dynamics (CFD) program Ansys Fluent 19.2, the equation mentioned above is solved using the finite volume approach with double precision. Using the SIMPLEC algorithm, the pressure-velocity coupling problem and the interpolation function problem are resolved, and the second-order upwind method is implemented. The criterion for convergence is set at 10E-6 for the energy equation and 10E-3 for the remaining equations.

2.6 Grid-Independent Test and Validation Model

The fuel cell model created in this work needed to be validated; thus, the simulated results were compared with simulated results that relied on Wang et al. [21] report with different stoichiometric ratios of the intake gas. This was done so that the model could be considered accurate. As a cell's current density grows, the cell's voltage typically decreases. The grid independence test depicted in Fig. 2 (a) was successfully carried out after an increase of 5% to the total mesh elements. As described in Fig. 2 (b), Across the ranges of current densities, the conclusions of the model are in agreement with the observed data.

3 Results and Discussion

3.1 Overall Cell Performance

Different tapered parallel FFCs' polarization and power density curves are depicted in Fig. 3 and 4, respectively, both with and without TCR and PMT considerations. Adjusting the $L_{I/O}$ for particular tapered parallel FFCs results in significant variation in the polarization and power density curves compared to conventional parallel FFCs. A reduced $L_{I/O}$ leads to a decrease in output cell voltage and power density at the same current density for a variety of tapered parallel FFCs with or without consideration of the TCR and the PMT, particularly at higher current densities. This concept is especially noticeable at higher current densities. Due to the larger contact area between the BPs and GDLs, the CHs and GDLs have less contact, making it harder to transport reactants from the CHs to the GDLs. According to the findings, a parallel FFC with a taper (from the intake to the exit) has a detrimental effect on the cell's performance. Increasing the $L_{I/O}$, on the other hand, always increases cell performance due to enhanced reactant transport due to a larger contact region between CHs and GDLs. This is true for particular tapered parallel FFCs even when the TCR and PMT are not considered (case 1).

Increased $L_{I/O}$ results in initially improved cell performance for CN5 ($L_{I/O}$ 1.0) and CN6 ($L_{I/O}$ 1.2) and then decreased performance for CN1 ($L_{I/O}$ 0.2) and CN2 ($L_{I/O}$ 0.4) for different tapered parallel FFCs take into account the PMT and the TCR. The trade-off between mass transfer, water removal, TCR, and PMT can explain this due to differences in the LI/O that occur for various tapered parallel FFCs. In most cases, a reversed taper parallel FFC with a modestly high LI/O ratio benefits the cell's performance. According to the findings, ignoring the TCR and PMT between GDLs and BPs for tapered parallel FFCs can result in a variation in numerical cell performance, leading to an incorrect optimization of tapered parallel FFCs. This variation in the simulated performance of the cell can lead to an incorrect optimization of tapered parallel FFCs.

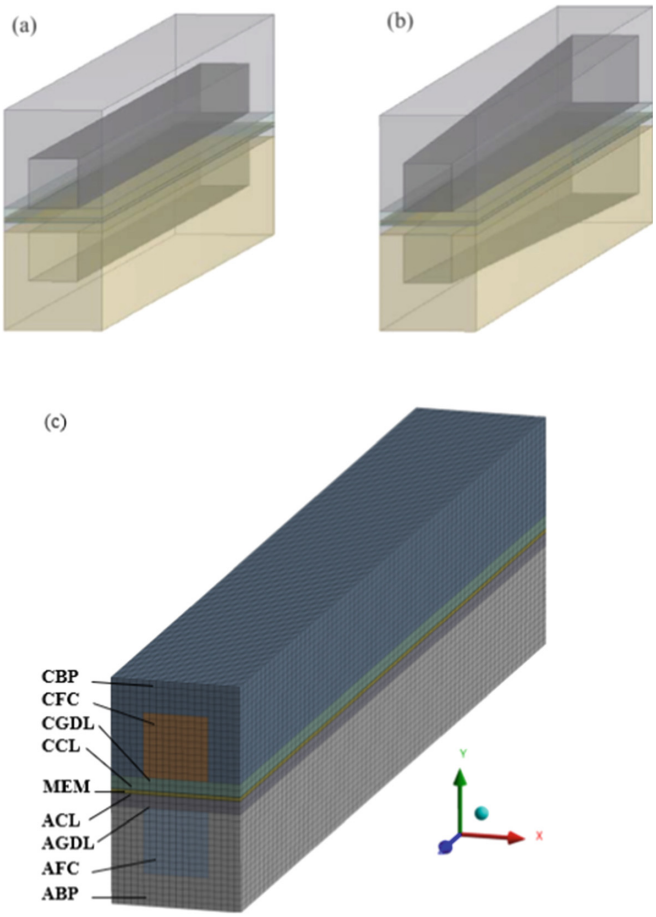

Fig. 1. Schematic of a PEM fuel cell with (a) conventional, (b) tapered parallel FFCs, and (c) parallel FFC fuel cell numerical domain and mesh generation.

Table 3. Grid independence test results.

No.	Grid number	Average current density/ A cm^{-2} ($V_{cell} = 0.60$ V)	Time consumed for 100 iteration (s)
1	496,000	0.74918	758
2	512,000	0.76787	792
3	544,000	0.72785	1052
4	560,000	0.75763	1102
5	592,000	0.73686	1193

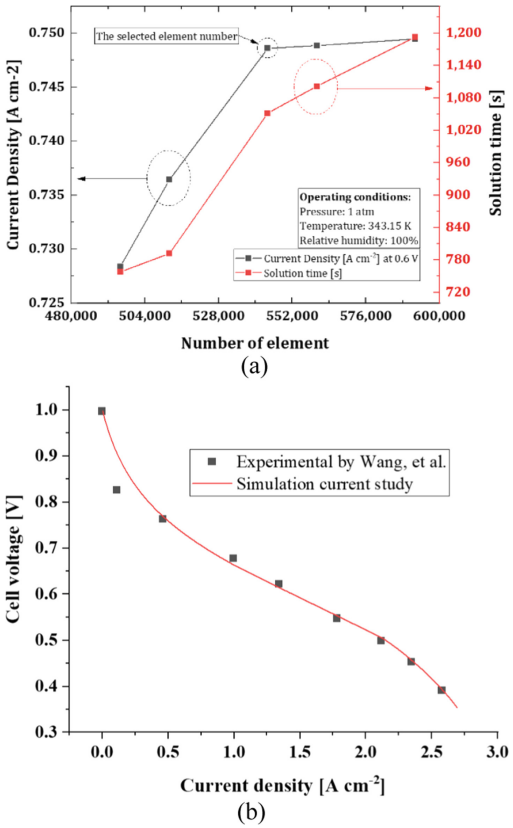

Fig. 2. (a) Current density grid independence evaluation at V = 0.60 V, (b) The polarization curves comparison for validation between numerical results of the present study with experiment values [21].

3.2 Oxygen Molar Concentration

Figure 5 illustrates the patterns of concentration of oxygen molar in the x-y planes of the fuel cell in the z-axis (direction of gas flow) approach for many tapered parallel FFCs when the cell voltage is set to 0.6 V. Due to oxygen consumption from the CCL's oxygen reduction process, the concentration of oxygen molar along the x-y planes of a fuel cell typically drops down the z-axis (ORR). Generally, having a high concentration of oxygen molar in the CGDL and CCL benefits the ORR rate in the CCL. On the other hand, having a high oxygen molar concentration does not necessarily suggest a high ORR rate. As depicted in Fig. 5, CN6 has a greater concentration of oxygen molar in the CGDL and CCL than in other examples. Its current density at a cell voltage of 0.6 V is significantly higher than that of CN5. This can be explained for CN6 by its relatively high TCR, which decreases charging transport and reduces the ORR rate inside the CCL. As a result, excess oxygen is left unused and tends to concentrate inside fuel cell electrodes.

Table 4. Model correlations of physicochemical transport equations for conservation. [10, 13, 14, 36, 41–44] [47].

Information	Source terms
Coefficient of gas effective diffusion (m^2 s^{-1})	$D_k^{eff} = D^{bulk}\varepsilon^{1.5}(T/343.15)^{1.5}(101325/P)$
Liquid water transport diffusivity (m^2 s^{-1})	$D_c = -(Kk_{kl}/\mu_1)(\partial p_c/\partial s)$ $p_c = \begin{cases} \sigma cos\theta\left(\frac{\varepsilon}{K}\right)^{0.5}\left(1.417(1-s) - 2.120(1-s)^2 + 1.262(1-s)^3\right)\theta < 90° \\ \sigma cos\theta\left(\frac{\varepsilon}{K}\right)^{0.5}\left(1.417s - 2.120s^2 + 1.262s^3\right)\theta > 90° \end{cases}$ $k_{rl} = s^{4.0}$
Dissolved water transport diffusivity	$D_\lambda^{eff} = \begin{cases} 3.1x10^{-7}\lambda\left(e^{0.28\lambda} - 1\right)e^{\left[-\frac{2346}{T}\right]}, 0 < \lambda \le 3 \\ 4.17x10^{-8}\lambda\left(1 + 161e^{-\lambda}\right)e^{\left[-\frac{2346}{T}\right]}, 3 < \lambda < 17 \\ 4.1x10^{-10}\left(\frac{\lambda}{25.0}\right)^{0.15}\left(1 + \frac{tanh(\lambda-2.5)}{1.4}\right), \lambda > 17 \end{cases}$ $\lambda_{eq} = \begin{cases} 0.043 + 17.81a_w - 39.85a_w^2 + 36.0a_w^3, 0 < a_w \le 1 \\ 14.0 + 1.4(a_w - 1), 1 < a_w \le 3 \\ 16.8, a_w > 3 \end{cases}$ $a_w = \frac{p^v}{p^{sat}} + 2s, p^v = X_{H_2O}\rho_g R_u T/M_{H_2O}$ $p^{sat} =$ $101325\text{x } 10^{-2.1794+0.02953(T-273.15)-9.1837x10^{-5}(T-273.15)^2+1.4454x10^{-7}(T-273.15)^3}$
Rate of electrochemical reaction (A cm^{-3})	$j_a = (1-s)A_s j_{0,a}^{ref} cos\theta\left(\frac{C_{H_2}}{C_{H_2}^{ref}}\right)^{0.5}\left(\exp\left(\frac{2F\alpha_a}{R_uT}\eta_a\right) - \exp\left(-\frac{2F\alpha_c}{R_uT}\eta_a\right)\right)$ $j_c = (1-s)A_s j_{0,c}^{ref} cos\theta\left(\frac{C_{O_2}}{C_{O_2}^{ref}}\right)^{1.0}\left(\exp\left(\frac{4F\alpha_a}{R_uT}\eta_c\right) - \exp\left(-\frac{4F\alpha_c}{R_uT}\eta_c\right)\right)$ $\eta_a = \phi_{e,a} - \phi_{mem,a}\eta_c = \phi_{e,c} - \phi_{mem,c} - (1.23 - 0.9 \times 10^{-3}\,(T\text{-}298.15) +$ $\frac{RT}{2F}\left(inp_{H_2}^{in} + \frac{1}{2}inp_{O_2}^{in}\right))$
Proton conductivity (S m^{-1})	$K_{mem}^{eff} = \begin{cases} (0.5139\lambda - 0.326)exp\left[1268\left(\frac{1}{303.15} - \frac{1}{T}\right)\right], membrane \\ \omega^{1.5}(0.5139\lambda - 0.326)exp\left[1268\left(\frac{1}{303.15} - \frac{1}{T}\right)\right], CLs \end{cases}$
Electro-osmotic drag coefficient	$n_d = \frac{25\lambda}{22}$

Table 5. The model's source terms for conservation equations [13, 14, 36, 42] [47].

Equations of conservation	Source terms
Mass	CHs, GDLs : $S_{\mathrm{m}} = -S_{\mathrm{vl}}$ ACL: $S_{\mathrm{m}} = -\frac{j_a M_{H_2}}{2\mathrm{F}} - S_{\mathrm{vl}}$, CCL : $S_{\mathrm{m}} = -\frac{j_c M_{H_2O}}{2\mathrm{F}} - \frac{j_a M_{O_2}}{4\mathrm{F}} - S_{\mathrm{vl}}$ kg m^{-3} s^{-1}
Momentum	CHs : $S_{\mathrm{u}} = 0$GDLs, CLs : $S_{\mathrm{u}} = -\left(\frac{\mu_{\mathrm{g}}}{K k_{\mathrm{rg}}} - \frac{1}{\varepsilon(1-s)}\overrightarrow{u_{\mathrm{g}}}\right)$
Species	CHs, GDLs : $S_{\mathrm{v}} = -S_{\mathrm{vl}}, S_{\mathrm{H_2}} = 0, S_{\mathrm{O_2}} = 0$ ACL : $S_{\mathrm{H_2}} = -\frac{j_a}{2\mathrm{F}} M_{\mathrm{H_2}}, S_{\mathrm{v}} = S_{\mathrm{dv}} M_{\mathrm{H_2O}} - S_{\mathrm{vl}}$, kg m^{-3} s^{-1} CCL : $S_{\mathrm{O_2}} = -\frac{j_a}{4\mathrm{F}} M_{\mathrm{O_2}}, S_{\mathrm{v}} = \frac{j_a}{2\mathrm{F}} M_{\mathrm{H_2O}} + S_{\mathrm{dv}} M_{\mathrm{H_2O}} - S_{\mathrm{vl}}$,
Liquid water	$S_{\mathrm{vl}} = \gamma_{\mathrm{cond}} \varepsilon (1-s) x_{\mathrm{H_2O}} \left(p^{\mathrm{v}} - p^{\mathrm{sat}}\right) M_{H_2O} / R_{\mathrm{u}} T, p^{\mathrm{v}} > p^{\mathrm{sat}}$ $S_{\mathrm{vl}} = \gamma_{\mathrm{evap}} \varepsilon s \rho \left(p^{\mathrm{v}} - p^{\mathrm{sat}}\right), p^{\mathrm{v}} < p^{\mathrm{sat}}$ kg m^{-3} s^{-1}
Dissolved water	ACL : $S_{\mathrm{d}} = -S_{\mathrm{dv}} - \frac{\rho_1 K_{\mathrm{mem}} P_1^{ACL} - P_1^{CCL}}{M_{\mathrm{H_2O}} \mu_1 \delta_{\mathrm{mem}} \delta_{\mathrm{CL}}}$, MEM : $S_{\mathrm{d}} = 0$ CCL : $S_{\mathrm{d}} = -S_{\mathrm{dv}} + \frac{\rho_1 K_{\mathrm{mem}} P_1^{ACL} - P_1^{CCL}}{M_{\mathrm{H_2O}} \mu_1 \delta_{\mathrm{mem}} \delta_{\mathrm{CL}}}$, $S_{\mathrm{dv}} = \frac{1.3EW}{\rho_{\mathrm{mem}}(\lambda_{\mathrm{eq}} - \lambda)}$ mol m^{-3} S^{-1}
Electron	ACL : $S_{\mathrm{e}} = j_a$; CCL : $S_{\mathrm{e}} = -j_e$ A m^{-3}
Proton	ACL : $S_{\mathrm{s}} = -j_a$; CCL : $S_{\mathrm{s}} = j_c$ A m^{-3}
Energy	CHs : $S_{\mathrm{T}} = 0$, BPs : $S_{\mathrm{T}} = \frac{i_{\mathrm{e}}^2}{K_{\mathrm{e}}^{\mathrm{eff}}}$, $GDLs$: $S_{\mathrm{T}} = \frac{i_{\mathrm{e}}^2}{K_{\mathrm{e}}^{\mathrm{eff}}} + hS_{\mathrm{vl}}$ ACL : $S_{\mathrm{T}} = \frac{i_{\mathrm{e}}^2}{K_{\mathrm{e}}^{\mathrm{eff}}} + \frac{i_{\mathrm{mem}}^2}{K_{\mathrm{mem}}^{\mathrm{eff}}} + hS_{\mathrm{vl}} + hS_{\mathrm{dv}} + j_{\mathrm{a}}\lvert\eta_{\mathrm{a}}\rvert + \frac{j_{\mathrm{a}} T \Delta S_{\mathrm{a}}}{2\mathrm{F}}$ W m^{-3} CCL : $S_{\mathrm{T}} = \frac{i_{\mathrm{e}}^2}{K_{\mathrm{e}}^{\mathrm{eff}}} + \frac{i_{\mathrm{mem}}^2}{K_{\mathrm{mem}}^{\mathrm{eff}}} + hS_{\mathrm{vl}} + hS_{\mathrm{dv}} + j_{\mathrm{c}}\lvert\eta_{\mathrm{c}}\rvert + \frac{j_{\mathrm{c}} T \Delta S_{\mathrm{c}}}{2\mathrm{F}}$

3.3 Liquid Water Saturation

At 0.6 V cell voltage, Fig. 6 shows the liquid water saturation patterns at the CCL and CGDL configurations through the CH for different tapered parallel FFCs with and without the TCR, the PMT, and the standard parallel FFC. Due to gas passage within the CHs, liquid water accumulates at the downstream CCL and CGDL interfaces. In addition, the liquid water saturation can be reduced when a larger $L_{I/O}$ is developed for tapered parallel FFCs without addressing the PMT and ECR. It indicates that a higher $L_{I/O}$ ratio is beneficial for water removal. However, CN5 and CN6 electrodes exhibited exceptionally low liquid water saturation and elevated $L_{I/O}$.

Table 6. Designed, transport and operating conditions in the model [13, 14, 36, 42] [47–49].

Parameters	Value
Porosity of CL, ε_{GDL}, ε_{CL}	0.6, 0.3
Contact angle of GDL, CL (°), θ_{GDL}, θ_{CL}	120, 100
Permeability of GDL, CL, MEM (m^2), K_{GDL}, K_{CL}, K_{MEM}	10^{-12}, 10^{-13}, 10^{-20}
Hydrogen bulk diffusivity ($m^2\ s^{-1}$), $D_{H_2}^{bulk}$	9.73×10^{-5}
Bulk diffusivity of oxygen ($m^2\ s^{-1}$), $D_{O_2}^{bulk}$	2.73×10^{-5}
Bulk diffusivity of vapor water ($m^2\ s^{-1}$), D_{v}^{bulk}	2.33×10^{-5}
Electronic conductivity of GDL, CL, BP (S m^{-1}), $Ke_{,GDL}$, $Ke_{,CL}$, $Ke_{,BP}$	50×10^3, 1.0×10^3, 8.0×10^4
Thermal conductivity of CL, MEM, BP (W $m^{-1}\ K^{-1}$), k_{CL}, k_{MEM}, k_{BP}	1.0, 0.95, 20.0
Thermal conductivity of GDL, MEM, BP (W $m^{-1}\ K^{-1}$), k_{CL}, k_{MEM}, k_{BP}	1.0, 0.95, 20.0
Liquid water density (kg m^{-3}), ρ_l	1.0×10^3
MEM density (kg m^{-3}), ρ_{MEM}	1980.0
Liquid water surface tension (N m^{-1}), σ	6.25×10^{-2}
Constant of universal gas (J $mol^{-1}\ K^{-1}$), R_u	8.314

(*continued*)

Table 6. (*continued*)

Parameters	Value
Faraday's constant (C mol^{-1}), F	96487.0
Ionomer equivalent weight (kg mol^{-1}), EW	1.1
Reference concentration (mol m^{-3}), $C^{ref}_{H_2}$, $C^{ref}_{O_2}$	56.4, 3.39
Condensation rate of vapour water constant (s^{-1}), γ_{cond}	5.0×10^3
Condensation rate og liquid water constant (s^{-1} pa^{-1}), γ_{evap}	10^{-4}
Anode/cathode transposition current density times specific area (A m^{-2}), $A_s j^{reff}_{0,a}/A_s j^{reff}_{0,c}$.	$1.0 \times 10^8 \exp\left(-1400\left(\frac{1}{T} - \frac{1}{343.15}\right)\right)/120 exp\left(-7900\left(\frac{1}{T} - \frac{1}{343.15}\right)\right)$
Anode/cathode transfer coefficient, a_a/a_c.	0.5/0.5
Entropy change of anode/cathode (J $mol^{-1}K^{-1}$), $\Delta S_a/\Delta S_c$	130.68/32.55
Coefficient of latent heat (J mol^{-1}), h	44900.0
The stoichiometric ratio of inlet gas ξ_a/ξ_c	2.0/3.0
Operating temperature (K)	343.15
Working pressure (atm)	1.0
Inlet relative humidity of anode/cathode, RHa/RHc	100%/100%
Current density reference (A cm^{-2}),i_{ref}	1.0×10^4

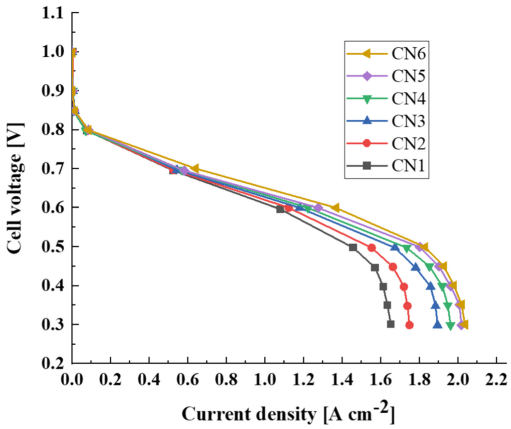

Fig. 3. Polarization curves for several parallel tapered FFCs

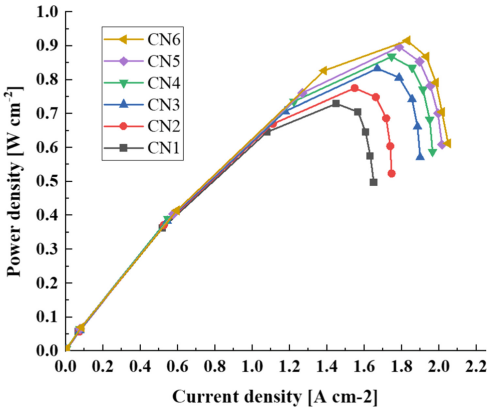

Fig. 4. Various power density curves for parallel tapered FFCs.

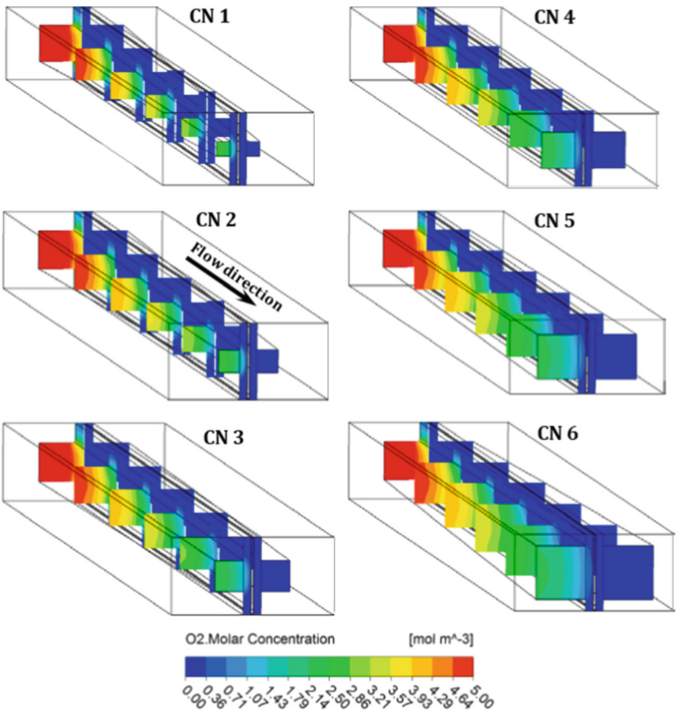

Fig. 5. Fuel cell molar concentration of oxygen in x, y, and z-axes (gas flow).

3.4 Current Density and Pressure Drop

Figure 7 shows the current density patterns on the center cross-section of the CCL for various tapered parallel FFCs without or with the TCR, PMT, and conventional parallel FFC at 0.6 V. For lower $L_{I/O}$, such as CN1-CN6 and traditional parallel FFC, the activation zone has a severe misdistribution of current density. By increasing the $L_{I/O}$, such as CN6, the current densities inside the CCL in the under-rib regions downstream of the CH are improved and more uniform. Tapered parallel FFCs with PMT and TCR exhibit lower CCL current densities than those without TCR because of the ohmic loss of fuel cells induced by PMT and TCR. Thus, tapered parallel FFC optimization will fail without the TCR. At 0.6 V, the pressure drop through the cathode channel for tapered parallel FFCs with or without TCR and standard parallel FFCs. Tapered parallel FFCs have lower cathode channel pressure drops due to higher $L_{I/O}$. A decrease in LI/O increases pressure drops significantly. Low cathode channel pressure reduces pumping effort to supply reactants to fuel cells, improving energy efficiency.

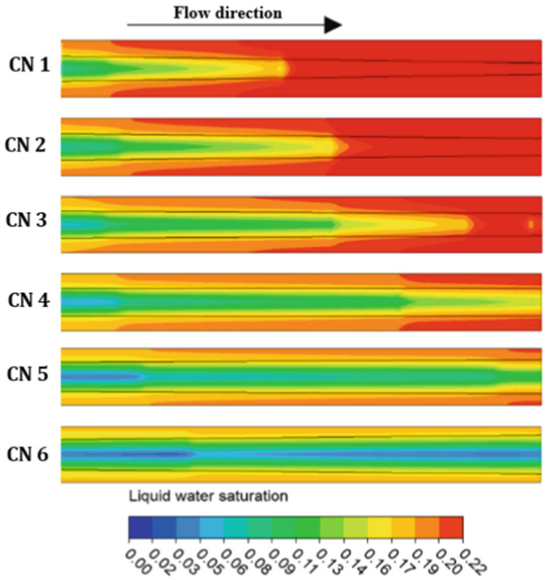

Fig. 6. The profile of liquid water saturation along the CH for different tapered parallel FFCs without and with TCR, PMT, and standard parallel FFC at 0.6 V.

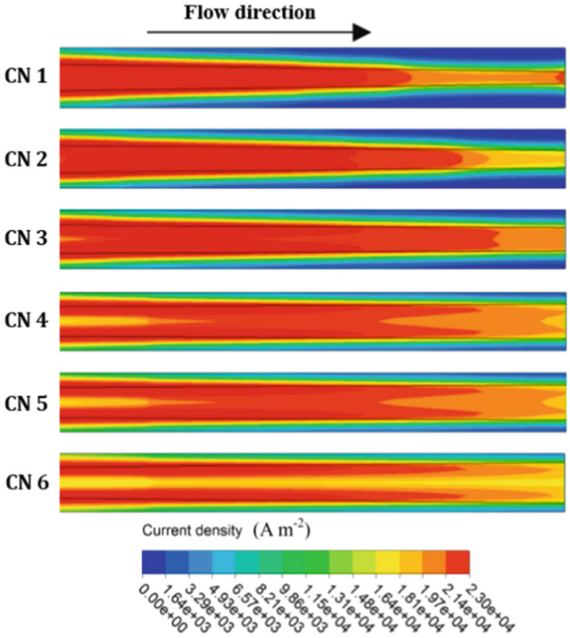

Fig. 7. Current density patterns at the middle CCL cross-section along the CH for different tapered parallel FFCs with and without the TCR, the PMT, and regular parallel FFC at 0.6 V.

4 Conclusions

This research uses tapered FFCs with TCR and PMT between gas diffusion layers and bipolar plates to increase PEM fuel cell performance. Numerical studies are performed using a three-dimensional multi-phase fuel cell model to examine the impact of the input side length to the outlet side length ($L_{I/O}$) on the distribution of internal physical processes like dissolved water content, oxygen transport, water removal, and current density. A comparison of tapered FFCs without and with TCR and PMT is also undertaken for a more specific summary as follows:

1. Due to the trade-off between mass transfer, water removal, PMT, and TCR produced by the fluctuation of LI/O, the cell performance of the tapered FFC with TCR and PMT initially increases and subsequently decreases. To obtain the optimal FFC design for fuel cells, the TCR and PMT should be considered while building an FFC with a smaller contact area between gas diffusion layers and bipolar plates.
2. The findings of the present computational research indicate that a greater LI/O for the tapered FFC, with or without the PMT and the TCR, is advantageous for water removal and oxygen transport, as well as for the homogenous distribution of oxygen and current densities inside fuel cells.
3. The optimal FFC decreases the oxygen molar concentration variation coefficient and the current density through the channel by approximately 6.5% and 16%, respectively. This indicates a more homogenous distribution of inside physical quantities within electrodes, which improves fuel cells' stable operation and lifetime.

Acknowledgement. This work was supported by the Technology Innovation Program (or Industrial Strategic Technology Development Program-The technology development on fuel cell electric propulsion system using Land Based Test Site) (RS-2022-00142947, The technology development on fuel cell electric propulsion system using Land Based Test Site) funded By the Ministry of Trade, Industry & Energy (MOTIE, Korea).

References

1. D. Zhou, A. Al-durra, F. Gao, A. Ravey, I. Matraji, and M. Godoy, "Online energy management strategy of fuel cell hybrid electric vehicles based on data fusion approach," vol. 366, pp. 278–291, 2017, https://doi.org/10.1016/j.jpowsour.2017.08.107.
2. J. P. Stempien and S. H. Chan, "Comparative study of fuel cell , battery and hybrid buses for renewable energy constrained areas," *J. Power Sources*, vol. 340, pp. 347–355, 2017, https://doi.org/10.1016/j.jpowsour.2016.11.089.
3. A. Kosakian, L. P. Urbina, A. Heaman, and M. Secanell, "Electrochimica Acta Understanding single-phase water-management signatures in fuel- cell impedance spectra : A numerical study," *Electrochim. Acta*, vol. 350, p. 136204, 2020, https://doi.org/10.1016/j.electacta.2020.136204.

4. Q. Wang *et al.*, "Numerical analysis of static and dynamic heat transfer behaviors inside proton exchange membrane fuel cell," *J. Power Sources*, vol. 488, no. December 2020, p. 229419, 2021, https://doi.org/10.1016/j.jpowsour.2020.229419.
5. A. P. Manso, F. F. Marzo, J. Barranco, X. Garikano, and M. Garmendia Mujika, "Influence of geometric parameters of the flow fields on the performance of a PEM fuel cell. A review," *Int. J. Hydrogen Energy*, vol. 37, no. 20, pp. 15256–15287, 2012, https://doi.org/10.1016/j.ijhydene.2012.07.076.
6. Y. Wang, B. Seo, B. Wang, N. Zamel, K. Jiao, and X. C. Adroher, "Fundamentals, materials, and machine learning of polymer electrolyte membrane fuel cell technology," *Energy AI*, vol. 1, p. 100014, 2020, https://doi.org/10.1016/j.egyai.2020.100014.
7. J. Zhao, Z. Tu, and S. H. Chan, "Carbon corrosion mechanism and mitigation strategies in a proton exchange membrane fuel cell (PEMFC): A review," *J. Power Sources*, vol. 488, no. January, p. 229434, 2021, https://doi.org/10.1016/j.jpowsour.2020.229434.
8. M. Ashrafi and M. Shams, "The effects of flow-field orientation on water management in PEM fuel cells with serpentine channels," *Appl. Energy*, vol. 208, no. 17, pp. 1083–1096, 2017, https://doi.org/10.1016/j.apenergy.2017.09.044.
9. A. Kumar and R. G. Reddy, "Effect of channel dimensions and shape in the flow-field distributor on the performance of polymer electrolyte membrane fuel cells," *J. Power Sources*, vol. 113, no. 1, pp. 11–18, 2003, https://doi.org/10.1016/S0378-7753(02)00475-5.
10. X. D. Wang, G. Lu, Y. Y. Duan, and D. J. Lee, "Numerical analysis on performances of polymer electrolyte membrane fuel cells with various cathode flow channel geometries," *Int. J. Hydrogen Energy*, vol. 37, no. 20, pp. 15778–15786, 2012, https://doi.org/10.1016/j.ijhydene.2012.04.028.
11. J. Bachman, M. Charvet, A. Santamaria, H. Y. Tang, J. W. Park, and R. Walker, "Experimental investigation of the effect of channel length on performance and water accumulation in a PEMFC parallel flow field," *Int. J. Hydrogen Energy*, vol. 37, no. 22, pp. 17172–17179, 2012, https://doi.org/10.1016/j.ijhydene.2012.08.023.
12. N. J. Cooper, A. D. Santamaria, M. K. Becton, and J. W. Park, "Investigation of the performance improvement in decreasing aspect ratio interdigitated flow field PEMFCs," *Energy Convers. Manag.*, vol. 136, pp. 307–317, 2017, https://doi.org/10.1016/j.enconman.2017.01.005.
13. X. Wang, Y. Qin, S. Wu, X. Shangguan, J. Zhang, and Y. Yin, "Numerical and experimental investigation of baffle plate arrangement on proton exchange membrane fuel cell performance," *J. Power Sources*, vol. 457, no. March, p. 228034, 2020, https://doi.org/10.1016/j.jpowsour.2020.228034.
14. Y. Yin, S. Wu, Y. Qin, O. N. Otoo, and J. Zhang, "Quantitative analysis of trapezoid baffle block sloping angles on oxygen transport and performance of proton exchange membrane fuel cell," *Appl. Energy*, vol. 271, no. March, p. 115257, 2020, https://doi.org/10.1016/j.apenergy.2020.115257.
15. N. Zehtabiyan-Rezaie, A. Arefian, M. J. Kermani, A. K. Noughabi, and M. Abdollahzadeh, "Effect of flow field with converging and diverging channels on proton exchange membrane fuel cell performance," *Energy Convers. Manag.*, vol. 152, no. May, pp. 31–44, 2017, https://doi.org/10.1016/j.enconman.2017.09.009.
16. X. Chen *et al.*, "Performance investigation on a novel 3D wave flow channel design for PEMFC," *Int. J. Hydrogen Energy*, vol. 46, no. 19, pp. 11127–11139, 2021, https://doi.org/10.1016/j.ijhydene.2020.06.057.
17. W. Li *et al.*, "Experimental and numerical analysis of a three-dimensional flow field for PEMFCs," *Appl. Energy*, vol. 195, pp. 278–288, 2017, https://doi.org/10.1016/j.apenergy.2017.03.008.

18. Y. Xu, L. Peng, P. Yi, and X. Lai, "Analysis of the flow distribution for thin stamped bipolar plates with tapered channel shape," *Int. J. Hydrogen Energy*, vol. 41, no. 9, pp. 5084–5095, 2016, https://doi.org/10.1016/j.ijhydene.2016.01.073.
19. C. Wang *et al.*, "Effect of height/width-tapered flow fields on the cell performance of polymer electrolyte membrane fuel cells," *Int. J. Hydrogen Energy*, vol. 42, no. 36, pp. 23107–23117, 2017, https://doi.org/10.1016/j.ijhydene.2017.07.136.
20. J. Lee *et al.*, "Innovative cathode flow-field design for passive air-cooled polymer electrolyte membrane (PEM) fuel cell stacks," *Int. J. Hydrogen Energy*, vol. 45, no. 20, pp. 11704–11713, 2020, https://doi.org/10.1016/j.ijhydene.2019.07.128.
21. Y. Wang, X. Wang, Y. Fan, W. He, J. Guan, and X. Wang, "Numerical Investigation of Tapered Flow Field Configurations for Enhanced Polymer Electrolyte Membrane Fuel Cell Performance," *Appl. Energy*, vol. 306, no. PA, p. 118021, 2022, https://doi.org/10.1016/j.apenergy.2021.118021.
22. H. Guo, H. Chen, F. Ye, and C. F. Ma, "Baffle shape effects on mass transfer and power loss of proton exchange membrane fuel cells with different baffled flow channels," *Int. J. Energy Res.*, vol. 43, no. 7, pp. 2737–2755, 2019, https://doi.org/10.1002/er.4328.
23. Y. Wang, Z. Xing, Z. Li, X. Wu, G. Wang, and W. Zhou, "Facile synthesis of high-thermostably ordered mesoporous TiO2/SiO2 nanocomposites: An effective bifunctional candidate for removing arsenic contaminations," *J. Colloid Interface Sci.*, vol. 485, pp. 32–38, 2017, https://doi.org/10.1016/j.jcis.2016.09.022.
24. M. Whiteley *et al.*, "A novel polymer electrolyte fuel cell flow-field: The through-plane array," *J. Power Sources*, vol. 442, no. September, p. 227218, 2019, https://doi.org/10.1016/j.jpowsour.2019.227218.
25. S. A. Atyabi and E. Afshari, "Three-dimensional multi-phase model of proton exchange membrane fuel cell with honeycomb flow field at the cathode side," *J. Clean. Prod.*, vol. 214, pp. 738–748, 2019, https://doi.org/10.1016/j.jclepro.2018.12.293.
26. J. Y. Jang, C. H. Cheng, W. T. Liao, Y. X. Huang, and Y. C. Tsai, "Experimental and numerical study of proton exchange membrane fuel cell with spiral flow channels," *Appl. Energy*, vol. 99, pp. 67–79, 2012, https://doi.org/10.1016/j.apenergy.2012.04.011.
27. S. R. Suseendiran, S. Pearn-Rowe, and R. Rengaswamy, "Development of cylindrical PEM fuel cells with semi-cylindrical cathode current collectors," *Int. J. Hydrogen Energy*, vol. 45, no. 17, pp. 10549–10558, 2020, https://doi.org/10.1016/j.ijhydene.2019.09.113.
28. Z. Saghali and J. Mahmoudimehr, "Superiority of a novel conic tubular PEM fuel cell over the conventional cylindrical one," *Int. J. Hydrogen Energy*, vol. 42, no. 48, pp. 28865–28882, 2017, https://doi.org/10.1016/j.ijhydene.2017.10.058.
29. J. M. Sierra, S. J. Figueroa-Ramírez, S. E. Díaz, J. Vargas, and P. J. Sebastian, "Numerical evaluation of a PEM fuel cell with conventional flow fields adapted to tubular plates," *Int. J. Hydrogen Energy*, vol. 39, no. 29, pp. 16694–16705, 2014, https://doi.org/10.1016/j.ijhydene.2014.04.078.
30. G. Cai, Y. Liang, Z. Liu, and W. Liu, "Design and optimization of bio-inspired wave-like channel for a PEM fuel cell applying genetic algorithm," *Energy*, vol. 192, p. 116670, Feb. 2020, https://doi.org/10.1016/J.ENERGY.2019.116670.
31. X. W. Zhang, X. J. Wang, X. Z. Cheng, L. Jin, J. W. Zhu, and T. T. Zhou, "Numerical analysis of global and local performance variations of proton exchange membrane fuel cell with different bend layouts and flow directions," *Energy*, vol. 207, p. 118141, Sep. 2020, https://doi.org/10.1016/J.ENERGY.2020.118141.
32. A. Iranzo, C. H. Arredondo, A. M. Kannan, and F. Rosa, "Biomimetic flow fields for proton exchange membrane fuel cells: A review of design trends," *Energy*, vol. 190, p. 116435, Jan. 2020, https://doi.org/10.1016/J.ENERGY.2019.116435.

33. Y. Cai, D. Wu, J. Sun, and B. Chen, "The effect of cathode channel blockages on the enhanced mass transfer and performance of PEMFC," *Energy*, vol. 222, p. 119951, May 2021, https://doi.org/10.1016/J.ENERGY.2021.119951.
34. V. Mishra, F. Yang, and R. Pitchumani, "Measurement and prediction of electrical contact resistance between gas diffusion layers and bipolar plate for applications to PEM fuel cells," *J. Fuel Cell Sci. Technol.*, vol. 1, no. 1, pp. 2–9, 2004, https://doi.org/10.1115/1.1782917.
35. P. Zhou, C. W. Wu, and G. J. Ma, "Contact resistance prediction and structure optimization of bipolar plates," *J. Power Sources*, vol. 159, no. 2, pp. 1115–1122, Sep. 2006, https://doi.org/10.1016/J.JPOWSOUR.2005.12.080.
36. T. Yoshizumi, H. Kubo, and M. Okumura, "Development of High-Performance FC Stack for the New MIRAI," *SAE Tech. Pap.*, no. 2021, Apr. 2021, https://doi.org/10.4271/2021-01-0740.
37. Y. Wang, C. Si, Y. Qin, X. Wang, Y. Fan, and Y. Gao, "Bio-inspired design of an auxiliary fishbone-shaped cathode flow field pattern for polymer electrolyte membrane fuel cells," *Energy Convers. Manag.*, vol. 227, no. August 2020, p. 113588, 2021, https://doi.org/10.1016/j.enconman.2020.113588.
38. D. A. G. Bruggeman, "Berechnung verschiedener physikalischer Konstanten von heterogenen Substanzen. I. Dielektrizitätskonstanten und Leitfähigkeiten der Mischkörper aus isotropen Substanzen," *Ann. Phys.*, vol. 416, no. 7, pp. 636–664, Jan. 1935, https://doi.org/10.1002/ANDP.19354160705.
39. Y. Wang, S. Wang, S. Liu, H. Li, and K. Zhu, "Three-dimensional simulation of a PEM fuel cell with experimentally measured through-plane gas effective diffusivity considering Knudsen diffusion and the liquid water effect in porous electrodes," *Electrochim. Acta*, vol. 318, pp. 770–782, 2019, https://doi.org/10.1016/j.electacta.2019.06.120.
40. S. Motupally, A. J. Becker, and J. W. Weidner, "Scholar Commons Scholar Commons Diffusion of Water in Nafion 115 Membranes Diffusion of Water in Nafion 115 Membranes," *J. Electrochem. Soc.*, pp. 3171–3177, 2000, https://doi.org/10.1149/1.1393879.
41. E. J. F. Dickinson and G. Hinds, "The Butler-Volmer Equation for Polymer Electrolyte Membrane Fuel Cell (PEMFC) Electrode Kinetics: A Critical Discussion," *J. Electrochem. Soc.*, vol. 166, no. 4, pp. F221–F231, Feb. 2019, https://doi.org/10.1149/2.0361904JES/XML.
42. T. E. Springer, T. A. Zawodzinski, and S. Gottesfeld, "Polymer Electrolyte Fuel Cell Model," *J. Electrochem. Soc.*, vol. 138, no. 8, pp. 2334–2342, Aug. 1991, https://doi.org/10.1149/1.2085971/XML.
43. B. Wang *et al.*, "A dot matrix and sloping baffle cathode flow field of proton exchange membrane fuel cell," *J. Power Sources*, vol. 434, Sep. 2019, https://doi.org/10.1016/j.jpowsour.2019.226741.
44. G. Zhang, B. Xie, Z. Bao, Z. Niu, and K. Jiao, "Multi-phase simulation of proton exchange membrane fuel cell with 3D fine mesh flow field," *Int. J. Energy Res.*, vol. 42, no. 15, pp. 4697–4709, Dec. 2018, https://doi.org/10.1002/ER.4215.
45. W. Z. Li, W. W. Yang, N. Wang, Y. H. Jiao, Y. Yang, and Z. G. Qu, "Optimization of blocked channel design for a proton exchange membrane fuel cell by coupled genetic algorithm and three-dimensional CFD modeling," *Int. J. Hydrogen Energy*, vol. 45, no. 35, pp. 17759–17770, 2020, https://doi.org/10.1016/j.ijhydene.2020.04.166.